AIAA AVIATION Forum
June 25-29, 2018, Atlanta, Georgia
2018 AIAA/CEAS Aeroacoustics Conference

10.2514/6.2018-2826

Dependence of High-performance Military Aircraft Noise on Frequency and Engine Power[1]

Kevin M. Leete[2]
Brigham Young University, Provo, UT 84602, USA

Alan T. Wall[3]
Air Force Research Laboratory, Wright-Patterson Air Force Base, OH 45433, USA

Kent L. Gee,[4] Tracianne B. Neilsen,[5]
Brigham Young University, Provo, UT 84602, USA

Michael M. James[6] and J. Micah Downing[7]
Blue Ridge Research and Consulting. Asheville, NC 28801, USA

To further understand the unique characteristics of military aircraft noise, the sound field in the vicinity of a tied-down F-35B was measured for various engine powers, from 25% to 150% Engine Thrust Request (ETR). Synchronous measurements along a linear ground array approximately parallel to the shear layer were used to image the entire field through multisource statistically optimized near-field acoustical holography (M-SONAH). The field in the direction of maximum radiation consists of multiple lobes in the spatiospectral domain, which are manifest as multiple local maxima in space for a fixed frequency or multiple peaks in the spectra at a fixed location. Multiple lobes are observed at non-afterburning and afterburning engine conditions. As frequency increases for a given engine power, lobes appear towards the sideline and shift aft until they disappear beyond the measurement aperture and new lobe(s) take their place. As engine power is increased at a fixed frequency, the forward-most lobe increases in its relative contribution to the field, which is a major contributing factor to the forward shift in overall directivity with increasing engine power. Field reconstructions and data in the forward direction outside of the region of maximum radiation show the presence of broadband shock-associated noise (BBSAN) for 75% ETR and above. Reconstructions along the nozzle lipline of the jet indicate the BBSAN originates from approximately the same region as the sources for the main radiation direction

Nomenclature

A	=	Hologram wave function matrix
BBSAN	=	Broadband shock-associated noise
c	=	Speed of sound (m/s)
CSM	=	Cross-spectral matrix
dz	=	inter-element spacing in z coordinate (m)
ETR	=	Engine Thrust Request

[1] Distribution A: Approved for public release, distribution unlimited. F-35 PAO Cleared 05-16-2018, JSF18-529
[2] Corresponding Author, Graduate Student, Dept. of Physics and Astronomy, N283 ESC, Provo, UT 84602, AIAA Student Member.
[3] Research Physicist, Battlespace Acoustics Branch, 2610 Seventh St. Bldg. 441, Wright-Patterson AFB OH 45433, AIAA Member.
[4] Associate Professor, Dept. of Physics and Astronomy, N283 ESC, Provo, UT 84602, AIAA Senior Member.
[5] Part-Time Professor, Dept. of Physics and Astronomy, N283 ESC, Provo, UT 84602, AIAA Member.
[6] Vice President and Senior Principal Engineer, 29 N Market St., Suite 700, Asheville, NC 28801, AIAA Member
[7] Senior Scientist, 29 N Market St., Suite 700, Asheville, NC 28801, AIAA Member

EWM = Equivalent wave model
H = Hermitian transpose operator
H_l^1 = Hankel function of the first kind of order l
i = Imaginary unit
k = Acoustic wavenumber (m^{-1})
k_r = Radial wavenumber (m^{-1})
k_z = Axial wavenumber (m^{-1})
MARP = Microphone array reference point
M-SONAH = Multisource statistically-optimized near-field acoustical holography
NAH = Near-field Acoustical holography
OTO = One-third octave
$\boldsymbol{p}$ = Complex pressure vector
$R_{\mathrm{A^H A}}$ = Regularized inverse of $\mathrm{A^H A}$
r, ϕ, z = Cylindrical coordinates
r_0 = Reference radius (m)
$\boldsymbol{r}_h$ = Coordinate vector of locations along the holography array
$\boldsymbol{r}_q$ = Coordinate vector of locations where the field is to be reconstructed
SVD = Singular value decomposition
T = Transpose operator
x, y, z = Cartesian coordinates (m)
$\boldsymbol{\alpha}$ = Reconstruction wave function matrix
ω = Angular frequency (s^{-1})
Δz = Total span of array in z coordinate (m)

I. Introduction

ALTHOUGH important insights are gained from laboratory-scale investigations of jet noise, some aspects of full-scale jet noise may not be reproduced by laboratory-scale measurements. Near-field acoustical holography (NAH), which was developed for three-dimensional imaging of noise fields [1, 2], has been used for laboratory jet noise measurements [3-5] and was recently adapted to full-scale measurements of the jet noise produced by military aircraft [6, 7]. NAH creates an equivalent wave model (EWM) for the field under examination, which can then be evaluated at any arbitrary point of interest. With a few simple assumptions, reliable estimations - within a certain spatial range of the sampled field - can be obtained to provide a high-resolution image of source and field characteristics [8]. NAH studies on jet noise from high-performance military aircraft have been successful in showing trends across frequency and engine conditions such as source extent and directivity [6, 7].

Wall *et al.* [9] used an advanced method of NAH called multisource statistically-optimized NAH (M-SONAH) to investigate the characteristics of the field in the vicinity of an F-35 operating at 100% Engine Thrust Request (ETR). Using a ground-based linear array as the input to the holography process, reconstructions over a large spatial region covering the near to far field in the area surrounding the aircraft were achieved. In the region of maximum radiation at single frequencies, multiple radiation lobes were observed, and as frequency increased, as many as four individual lobes emerge in the forward direction, move aft, and submerge back into the overall field. Evidence of broadband shock associate noise (BBSAN) was also observed as a lobe propagating in the forward direction.

Multilobe radiation is a feature of military aircraft jet noise that is seen in several datasets [7, 10-17], though no conclusive explanation of its cause has been given. These lobes are described as either multiple peaks in the spectra at a given measurement location or as multiple local maxima in space across the array when plotting a single frequency. Tam and Parrish [11] sought to explain dual spectral peaks shown in prior one-third octave band spectra in terms of indirect combustion noise sources that originate from within the nozzle. Liu [18-20] (using large-eddy simulations of cold and heated jets) show far-field evidence for at least two noise mechanisms with different directivities. Long [4] (using NAH to image the source from heated lab-scale jet) shows striation patterns in the spatial/spectral domain of the source. Orthogonal decompositions of NAH field reconstructions [21] and beamforming equivalent sources [22] suggest that multiple lobes are partially incoherent. Swift *et al.* [23] have performed an extensive correlation and

coherence analyses on the same dataset presented in this paper that verifies the mutual partial incoherence of the lobes. They also show correlation between the main radiation lobe in the aft direction and BBSAN in the forward direction, which suggests that shock cell interactions could be a contributor to these multilobe effects.

The purpose of the current study is to use M-SONAH, which was developed specifically for the use of imaging the field produced in the presence of a ground reflection, to reconstruct the sound field produced by a tied-down F-35 aircraft running across various engine conditions. Trends in observed multilobe and BBSAN phenomena across engine power are presented in a large area surrounding the jet for select narrowband frequencies. The measured and reconstructed fields show that the noise in the region of maximum radiation is a superposition of multiple spatiospectral lobes, whose interactions are the driving force behind trends across frequency and engine power. Previous observations of a "dual-peak" or multi lobe phenomena in Refs. [7, 11, 15, 16] appear to be subsets of the more complete picture described herein.

II. F-35 Measurement

This section discusses the measurement of the F-35 with a brief analysis of the OASPL and spectra gathered from a 71-element ground array placed approximately parallel to the shear layer.

A. Setup

An extensive measurement of the A and B variants of the F-35 was performed at Edwards Air Force Base in 2013 [10]. They were tied down to a concrete run up pad while the engine was cycled through various engine conditions, from 13% ETR up through 150% ETR. Engine powers greater than 100% ETR is due to the addition of afterburner. Each variant had a Pratt & Whitney F135 afterburning turbofan engine (the F135-PW-600 in the case of the F-35B discussed here), which can achieve up to 43,000 lbs. thrust. The nozzle of the engine was 2.0 m from the ground and had a nominal 1 m diameter, though the exact nozzle diameter changed with engine condition. The coordinate system, illustrated in Fig. 1, used in this study is centered on the nozzle exit as the origin with the jet plume faced down the positive z axis. The distance from the jet centerline is the x axis, and y is the height above the ground. A useful coordinate is the jet inlet angle θ, which is measured from the direction of the jet inlet ($-z$ direction) around a microphone array reference point (MARP) which was located at $z = 7.5$ m for the B variant. The array was laid out to the left side of the aircraft as shown in Ref [10], though for ease of plotting and consistency with previous NAH studies, all plots here are mirrored to show it on the right side of the aircraft.

Over 350 microphones were deployed from the vicinity of the shear layer out to 1200 m from the MARP [10]. This study focuses on a subset of these arrays. The first is a 32 m long, 71-element (0.45 m inter-element spacing) linear ground array placed approximately parallel to the shear layer, which is used as the input to the holography processing and is referred to as the holography array. The second is a near-field line consisting of four ground microphones placed closer to the jet plume. The remaining arrays used in this study are arcs of microphones at various heights above the ground with radii of 19, 29, 38 and 76 m from the MARP. These latter arrays are used for NAH validation. Fig. 1 shows a schematic for the test geometry with the coordinate system, arrays (the 76 m array is omitted for convenience), as well as location of the F-35B. Ref. [10] states that there is little variation in level between the recorded fields of the A and B variants, so for simplicity this study uses data collected from the B variant that should be sufficiently representative of both.

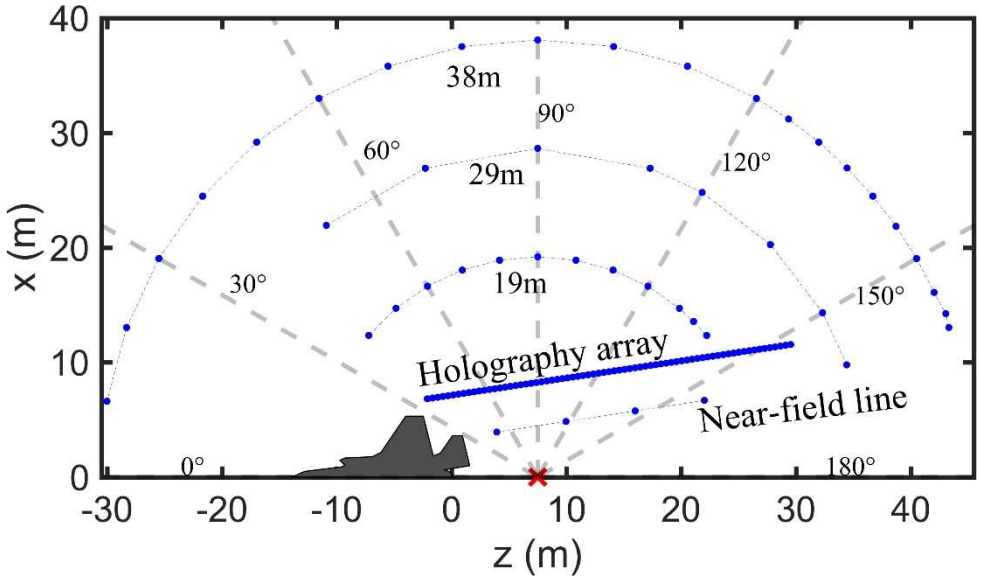

Fig. 1 Measurement array setup for the F-35 B. The red x is the microphone array reference point (MARP) which was 7.5 m behind the nozzle. Microphone locations are the blue dots. Several arcs with radii larger than 38 m are included in the measurement but are not pictured here for convenience.

B. Measured Data

The measured data along the 71-microphone holography array gives significant insight into trends across engine condition in the overall field. Fig. 2 shows the measured overall sound pressure levels at each point along the holography array. As engine power increases from 25-75% ETR, the radiated sound pressure levels drastically increase and the spatial distribution of energy becomes more directional. As engine condition varies from 75% to 150% ETR, the increase in level becomes less drastic and the shape remains similar, though becoming less peaked at afterburning conditions. The directivity (the relative concentration of energy in a given direction) shifts more towards the sideline as engine power increases, and there is an unexpected increase in level (at 50% ETR and above) at about $z = 22$ m. Additionally, and especially at 50% ETR, it appears as though the array was not long enough to completely capture the shape of a secondary local maximum.

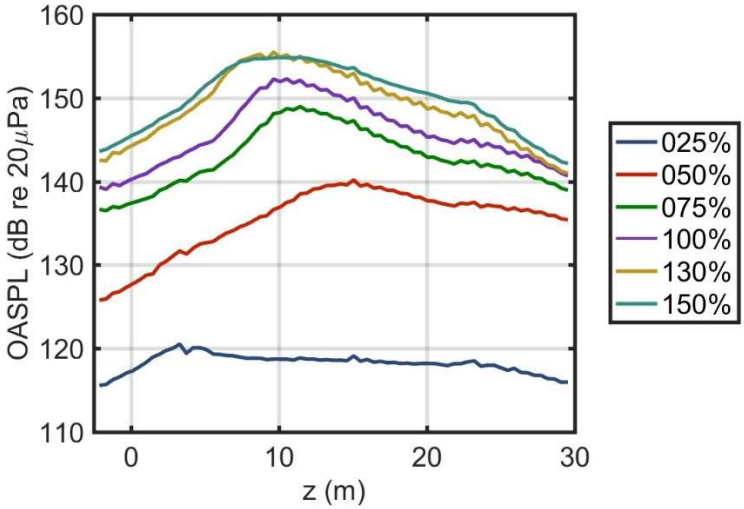

Fig. 2 OASPL across the holography array for several F-35B engine conditions, given in ETR.

The narrowband spectrum at each microphone gives important insight into the structure of the noise field. Fig. 3 shows the narrowband sound pressure levels for frequencies between 30 and 700 Hz (spacing of 3 Hz) for each microphone along the array. Each pane of Fig. 3 shows the data for an ETR (specified above the pane). Each level map is normalized to its peak, which is displayed above that pane. The color bar on the right (shared between panes) show the relative levels. As with the overall levels in Fig. 2, the peak levels in Fig. 3 increase dramatically from 25% ETR to 75% ETR then less from 75% to 150% ETR. At 25% ETR, the left portion of the array ($z < 10$ m) appears to be dominated by engine noise. At 50% ETR and above, the jet noise dominates the whole array. For engine conditions at 75% ETR and above, radiation in the forward direction is observed between 300-700 Hz, which analyses in Refs. [12, 13] show to be BBSAN.

The most prominent features of the spatiospectral plots in Fig. 3 is the presence of multiple lobes in the space – frequency domain. There appears to be two lobes at 25% ETR, four lobes between 50% ETR and 130% ETR and five at 150% ETR. Deciphering the exact number of lobes is an ongoing research problem, with different methods such as the coherence [23] being employed. For this preliminary work, the easily -discernable patterns of minima and maxima in the spectra as seen in Fig. 3 are used.

The peak level of each lobe appears to have a consistent location in the spatiospectral domain across engine conditions, though their extent, exact shape, and individual contributions to the field differ greatly. A clear example is the difference between the 50% ETR and 75% ETR engine conditions, where lobe 4 is just barely visible in the 50% ETR case but is a strong contributor to the 75% ETR case. This explains the difference between the 50% ETR and 75% ETR OASPL plots in Fig. 2 as well; the significant addition of upstream energy in the third and fourth lobes appears to be the driving force in not only the increase in level but also the forward shift in directivity. Qualitatively, it appears that the total field is a superposition of these lobular structures, which implies some incoherence between the lobes. This has been seen by Harker *et al.* [16] for a similar aircraft and is currently being investigated in Ref. [23]. These observations seem to show that what has been previously lumped into "large-scale turbulent structure noise" may actually be a superposition of several noise generation mechanisms, or the same mechanism originating from different locations. More research is needed to investigate these questions.

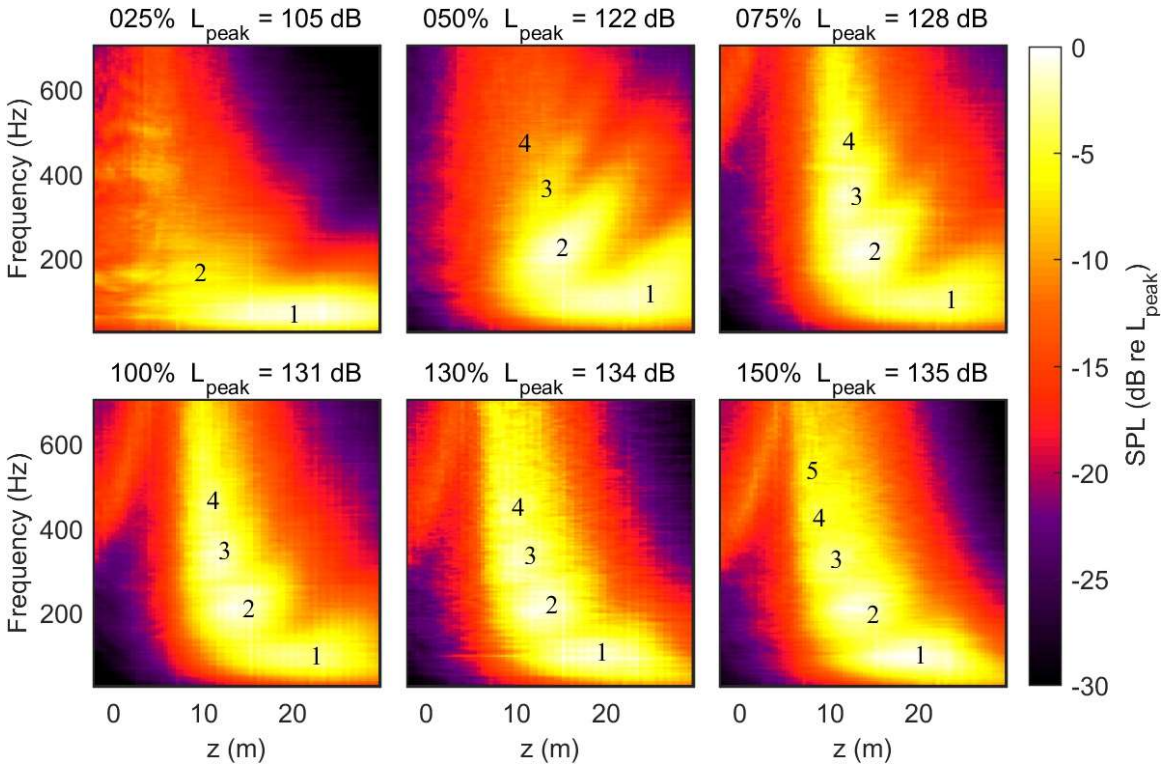

Fig. 3 Spatiospectral maps of normalized sound pressure level on the holography array as a function of distance from nozzle (z) and frequency. The numbers are used to identify the several spatiospectral lobes.

III. M-SONAH Method

This section discusses the procedure used to apply M-SONAH to the F-35 measurement described in Sec. II to reconstruct the pressure field in the area surrounding the aircraft. Part A discusses the step-by-step procedure which applies the work of Ref [24] to this measurement. Part B is a discussion on the limits on reconstruction accuracy, building on the work of Ref [8].

A. M-SONAH Procedure

The adaptation of NAH used in this study to predict the noise field of a tied-down high-performance military aircraft was developed by Wall *et al.* [24]. It is called multisource statistically-optimized near-field acoustical holography (M-SONAH) because it modifies the traditional SONAH algorithm [25] to use a two-source model: one along the jet centerline and an image source equidistant from but below the ground to account for the ground reflection. Each source has a corresponding set of cylindrical basis functions, which makes up the EWM of the field. The data from the holography array are the input to the M-SONAH algorithm, which includes these steps:

1. Extract frequency-dependent complex pressures from recorded pressure waveforms

To obtain the frequency-dependent complex pressures for all locations and engine conditions, the recorded 30-second time waveforms are split into multiple blocks with a 50% overlap, windowed with a Hann function, then the Fourier transform is applied to each block. Several organizations and different data acquisition systems with different sampling frequencies were involved in the simultaneous measurement of all the channels [10], so for this study the block size was chosen for each different sampling rate such that the resultant frequency resolution was a constant 3 Hz. This gives a single complex pressure value per block, per frequency. The remaining steps are done on a frequency-by-frequency basis.

2. Perform a partial field decomposition (PFD) to generate mutually incoherent partial fields

NAH can only deal with a coherent input hologram, but the jet noise field is only partially coherent. To overcome this, the input is decomposed into mutually incoherent, but self-coherent, fields that can be processed independently, then summed energetically at the end of the process to reproduce the total field [26]. A cross-spectral matrix (CSM, a matrix where each diagonal element is an autospectrum and each off diagonal element is the crossspectrum of that microphone pair) of the input array is calculated then a singular value decomposition (SVD) is done on the CSM. Each singular vector of the SVD scaled by its corresponding singular value yields a set of partial fields. The number of partial fields generated is equal to the number of elements in the input array. Since each partial field is processed individually, and the final reconstructed field is a sum of all the processed partial fields, a "filtering" of sorts can be done by only using the most energetic partial fields. In this study for each frequency of interest, as many partial fields were kept as were required to reconstruct 99.9% of the total energy present in the input hologram. For lower frequencies, this means that as few as four partial fields were used, and for higher frequencies, as many as 40. This substantially decreased computation time. Because the highest order partial fields generally had higher amplitudes towards the edges of the array, the 0.1% of energy removed generally causes the field at the edges of the array to be slightly underestimated.

3. Numerically extrapolate each partial field beyond the measurement aperture

The SONAH algorithm was originally developed to reduce errors caused by having a measurement that was not significantly larger than the source [25]. For this experiment, the 32-m aperture is not large enough to capture all the pertinent energy for the lowest frequencies, especially at the lowest engine conditions. This causes the finite-aperture effects to become significant even with the SONAH algorithm. The two largest sources of error were wraparound error and leakage of high wavenumbers due to a truncated field at the end of the array. Wraparound error is solved easily by sufficiently zero padding the edges of the input hologram so that it is much larger than the area in which the reconstructions are made. High wavenumber leakage is harder to solve, especially for low frequencies where the main radiation lobe is only partially covered by the array aperture. To reduce this effect, linear forward prediction was implemented to estimate values for the complex pressure of the field at locations beyond the measured aperture of the input array. In linear forward prediction, the coefficients of a polynomial are determined from existing data, the

polynomial is used to predict one point beyond the original aperture, and then the new point is included to make a new polynomial to represent the data, which is then used to estimate one more point beyond the aperture. This process is iterated until the field is extended the desired amount. This method was used for previous studies [27] because it was simple and sufficient , though potentially more robust methods exist [28].

A challenge with extending the aperture via linear forward prediction is that it is done on each partial field individually. The singular vectors produced by the SVD resemble oscillating functions across space (similar to modes on a string). If a high-order partial field is extended beyond the aperture, then its relative contribution to the overall field than is greater than the more important (energetic) first few partial fields, which often monotonically decrease from the maxima in the middle of the array towards the edge. This, combined with forward linear prediction's tendency to produce extraneous oscillations [27], makes the extension of the field only accurate for a short distance outside of the array. To enforce a graceful taper to zero and reduce the effect of extraneous oscillations outside the original aperture, a Tukey window is applied to the magnitude of the complex pressures along the extended input array. The window has a value of one inside the array that decays to a value of zero within an ad-hoc value of one acoustic wavelength of the edge of the array. Extending the aperture with the window provides zero padding as well. For this measurement geometry, the aperture is extended approximately 68 m on either side of the array, which is needed to eliminate wraparound error for 32 Hz. These errors could be significantly reduced if simultaneous measurements in the line of the holography array but farther downstream could be used to inform the aperture extension to create a more realistic extension of the field.

4. Formulate the EWM of the jet in the run-up pad environment and solve for pressure at desired reconstruction locations

The EWM methodology used in the M-SONAH algorithm is described in detail in Refs. [7, 24]. For this case, the EWM uses one set of cylindrical wave functions centered on the jet centerline and a second set centered on the image source below the ground to model the reflection. The basis function for outward propagation are

$$\psi_{l,k_z(r,\phi,z)} \equiv \frac{H_l^1(k_r r)}{H_l^1(k_r r_0)} e^{il\phi} e^{ik_z z}, r \geq r_0 \tag{1}$$

where r, ϕ, and z are the radial, azimuthal, and axial spatial coordinates, respectively; $H_l^1$is the lth-order Hankel function of the first kind; i is the imaginary unit; $r_0$is some small reference radius (traditionally the assumed source radius) [29]; and $k_z$is the axial wavenumber. The values of k_z were regularly spaced between $-\frac{\pi}{\mathrm{d}z}$ and $\frac{\pi}{\mathrm{d}z}$ in steps of $\frac{\pi}{\Delta z}$, where dz is the interelement spacing of the arrary in z and Δz is the total span of the array in z. The radial wavenumber is then

$$k_r = \begin{cases} \sqrt{k^2 - k_z^2} & \text{for } |k| \geq |k_z|, \\ i\sqrt{k_z^2 - k^2} & \text{for } |k| < |k_z|, \end{cases} \tag{2}$$

where $k = \omega/c$ is the acoustic wavenumber, ω is the angular frequency, and c is the speed of sound. The jet centerline is the line defined by $x = 0$ m and $y = 2.0$ m and the image jet centerline at $x = 0$ m, $y = -2.0$ m. The vector $\boldsymbol{r}_h$ is the position vector of all the points on the holography array, and $\boldsymbol{r}_q$ is the position vector of the points where the field is desired to be reconstructed. Equations 3 and 4,

$$\boldsymbol{r}^1 = \left(\sqrt{x^2 + (y + 2\mathrm{m})^2}, \tan^{-1}\left(\frac{y + 2\mathrm{m}}{x}\right), z\right) \tag{3}$$

$$\boldsymbol{r}^2 = \left(\sqrt{x^2 + (y - 2\mathrm{m})^2}, \tan^{-1}\left(\frac{y - 2\mathrm{m}}{x}\right), z\right) \tag{4}$$

show how the $\boldsymbol{r} = (r, \phi, z)$ coordinate vector is created for the two sources from the Cartesian coordinates of Fig. 1. Superscripts 1 and 2 denote whether it is the first (above ground) or second (below ground) coordinate system.

The total EWM is then created by evaluating all the ψ's at each measurement point and each reconstruction point. They are combined into the matrices $\mathbf{A}$ and $\boldsymbol{\alpha}$,

$$\mathbf{A}^1 = \begin{pmatrix} \psi_{\mathrm{k_{z1}}}(\boldsymbol{r}_h^1) & \dots & \psi_{\mathrm{k_{zM}}}(\boldsymbol{r}_h^1) \end{pmatrix}, \ \boldsymbol{\alpha}^1 = \begin{pmatrix} \psi_{\mathrm{k_{z1}}}(\boldsymbol{r}_q^1) & \dots & \psi_{\mathrm{k_{zM}}}(\boldsymbol{r}_q^1) \end{pmatrix}, \tag{5,6}$$

$$\mathbf{A}^2 = \begin{pmatrix} \psi_{k_{z1}}(\boldsymbol{r}_h^2) & \cdots & \psi_{k_{zM}}(\boldsymbol{r}_h^2) \end{pmatrix},\ \boldsymbol{\alpha}^2 = \begin{pmatrix} \psi_{k_{z1}}(\boldsymbol{r}_q^2) & \cdots & \psi_{k_{zM}}(\boldsymbol{r}_q^2) \end{pmatrix}, \tag{7,8}$$

$$\mathbf{A} = \begin{pmatrix} \mathbf{A}^1 \\ \mathbf{A}^2 \end{pmatrix}, \text{ and } \boldsymbol{\alpha} = \begin{pmatrix} \boldsymbol{\alpha}^1 \\ \boldsymbol{\alpha}^2 \end{pmatrix} \tag{9}$$

where the number of columns in **A** is equal to the number of wavefunctions used in this model (in this case the number of discrete k_z values), and the number of rows is equal to twice the number of measurement points in $\boldsymbol{r}_h$. $\boldsymbol{\alpha}$ has the same number of columns as **A**, but with rows equal to twice the number of points in $\boldsymbol{r}_q$.

At this point, the M-SONAH process is the same as SONAH, where the vector of pressure reconstructions $\boldsymbol{p}(\boldsymbol{r}_q)$ is given in terms of the transpose of the vector of hologram pressures $\boldsymbol{p}^T(\boldsymbol{r}_h)$ as

$$\boldsymbol{p}(\boldsymbol{r}_q) = \boldsymbol{p}^T(\boldsymbol{r}_h)\mathbf{R}_{\mathbf{A}^{\mathrm{H}}\mathbf{A}}\mathbf{A}^{\mathrm{H}}\boldsymbol{\alpha}, \tag{10}$$

where the superscript H is the Hermitian transpose and $\mathbf{R}_{\mathbf{A}^{\mathrm{H}}\mathbf{A}}$ is the regularized inverse of $\mathbf{A}^{\mathrm{H}}\mathbf{A}$. Regularization was performed using a modified Tikhonov filter with the generalized cross validation procedure for the selection of the regularization parameter as outlined in Ref [30]. The reconstructed pressures for each partial field are then energetically summed to obtain the final answer for each frequency. All levels shown in this paper for specific frequencies are scaled as if these frequencies were extracted from an autospectrum with units of Pa^2.

B. Reconstruction Accuracy

A previous study [8] calculated the errors in M-SONAH reconstructions of the F-35B field, which showed that the region of small error is dependent upon the spatial aperture of the holography array. Propagation errors from the holography array to arcs with 19, 29, 38 and 76 m radii were less than 2 dB between $\theta = 50°$ and $\theta = 150°$. However, because of the sparse sampling of the field by these arrays, it is difficult to say conclusively if the reconstructed field in this angular aperture always matches the actual field. To investigate where artifacts of the M-SONAH procedure applied to this measurement geometry are minimal, a simple numerical source was created along the jet centerline and generated complex pressures for several narrowband frequencies (33, 63, 81, 99, 126, 162, 201, 249, and 315 Hz) at all locations in the field. The M-SONAH procedure was applied to an input hologram (same spatial location as the F-35 Measurements) and field reconstructions were compared to the numerical field. Similar to the reconstructions of the aircraft data, there is region of low error (less than 2 dB) in the angular aperture covered by the input array. An example of this analysis for two frequencies is shown in Fig. 3 of Ref [8].

By simultaneously looking at the error of the M-SONAH reconstructions at the sparse locations measured in the field and 2-dB error contours for the numerical reconstructions, a conservative estimate of a region of good fit for the frequencies mentioned previously is established. A line is drawn from the edges of the holography array outward to select microphone positions at the 19, 38, and 76 m arcs. On the left of the main radiation lobe, the boundary points are chosen as $\theta = 50°$ for the 19, 38, and 76 m arcs; on the right, $\theta = 140°$ for the 38 m arc and $\theta = 130°$ for the 76 m arc (the 19 m arc did not extend far enough on the right-hand side). The resulting lines are continued from the edges of the holography array inward to the nozzle lipline to the spatial region that contains the top 6 dB of reconstructed levels. This region is only for frequencies less than 400 Hz, where aliasing is not apparent in the reconstructions. Within this region, the only significant errors should be due to inability to fully model ground interference effects due to the extended, partially coherent, volumetric source. To avoid ground interference effects, reconstructions for this study are done along the ground plane, or $y = 0$ m.

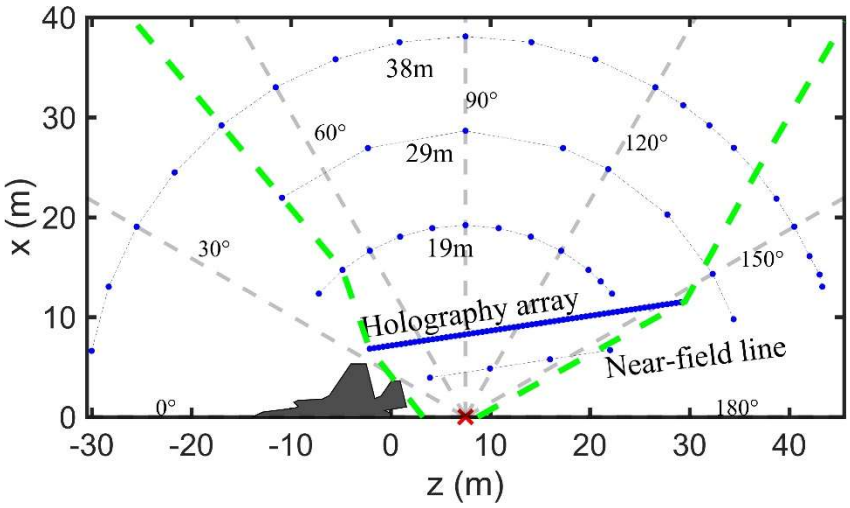

Fig. 4 Example of the region of good fit for reconstructions at frequencies less than 400 Hz superimposed on Fig. 1.

IV. Results and Discussion

This section shows the reconstructed field on a plane along the ground in the area surrounding the aircraft. Part A discusses the spatial and frequency regions where reliable reconstructions are obtained. Part B discusses the reconstructions that were made along the nozzle lipline of the jet to give insight into acoustic source characteristics of the jet plume. Part C shows reconstructions made to the field in the region to the side of the aircraft to characterize BBSAN directivity and apparent source region. Part D looks at the region of maximum radiation in the aft direction, and uses the field sound level maps to characterize the multiple radiation lobes, tracking their development across frequency and engine power. Part E compares these results to previous studies of similar military aircraft as well as a numerical simulation of a laboratory scale jet.

A. General results

The errors of the M-SONAH reconstruction along the holography array are displayed in Fig. 5 for all engine conditions. Errors occur at very low frequencies where the method overestimates the level and at frequencies above 400 Hz where the levels are underestimated. The high-frequency level underestimations are due to spatial aliasing, where the trace wavelength of the radiation along the array is smaller than twice the microphones spacing in the array. The spatial aliasing at frequencies above 400 Hz causes a reallocation of energy to a lobe with a directivity 90° off from main radiation, which would represent a source downstream propagating upstream. The upstream region of $z <$ 10 m maintains a smaller error for frequencies above 400 Hz until the aliased lobe causes an overestimation of the levels there (particularly at 75% and 100% ETR above 500 Hz. For investigations into the shape of the main radiation lobes as a function of engine condition, only frequencies less than 400 Hz are considered to avoid aliasing problems.

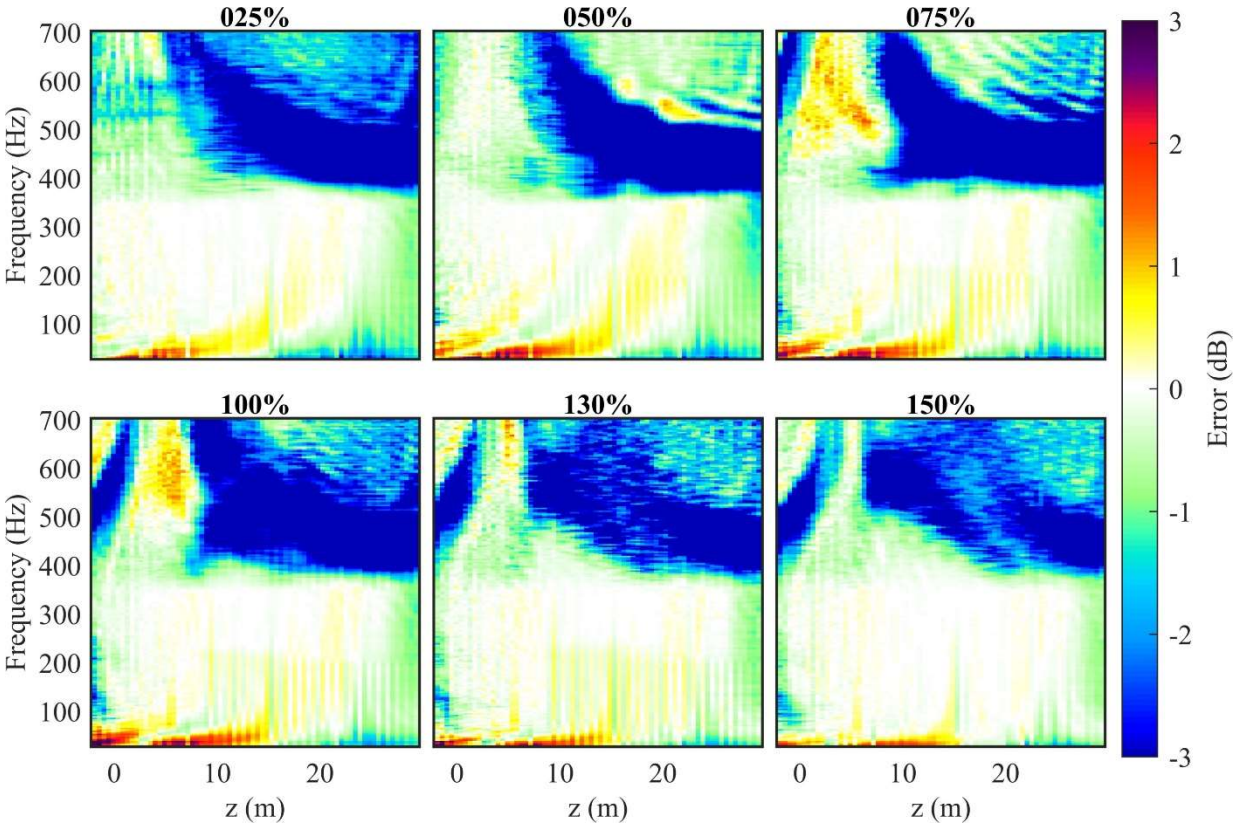

Fig. 5 Error of the M-SONAH reconstruction along the input holography array as a function of frequency for six engine conditions.

The true power of the MSONAH method is manifest in its ability to reconstruct the field at any arbitrary location. Fig. 6 shows reconstructions of the field to points in the ground plane ($y = 0$) for two representative frequencies and engine conditions. The top row corresponds to 162 Hz and the bottom row to 354 Hz. The two columns represent two engine conditions, on the left, an intermediate condition (75% ETR) and on the right, the maximum afterburning condition (150% ETR). The color contour maps show the sound pressure level at each point, the black line is the location of the holography array, the green dashed lines represent the region of expected good fit as discussed in section III.B, and the gray outline is the approximate position of the aircraft. In general, the reconstructions show field trends to be expected of jet noise, with the maximum radiation beaming at a large aft angle, and lower levels to the sideline. Due to windowing applied during the aperture extension (Sec III.A.3), the hologram pressures (and thus the field around them) are pinned to zero to the extreme left and right portions of the plot.

The most apparent features at these frequencies are the multiple radiation lobes. At 75% ETR and 162 Hz, two lobes are present with distinct directivities and apparent source locations, and at the same frequency but 150% ETR, the lobes rotate to a more forward directivity, have a higher level, and overlap more. The same trend (though less clear) can be seen at 354 Hz. Edge effects due to the finite window can be seen just outside of the green dashed lines, particularly at 162 Hz and 75% ETR where the edge effects corrupt the shape of the lobe as it passes through.

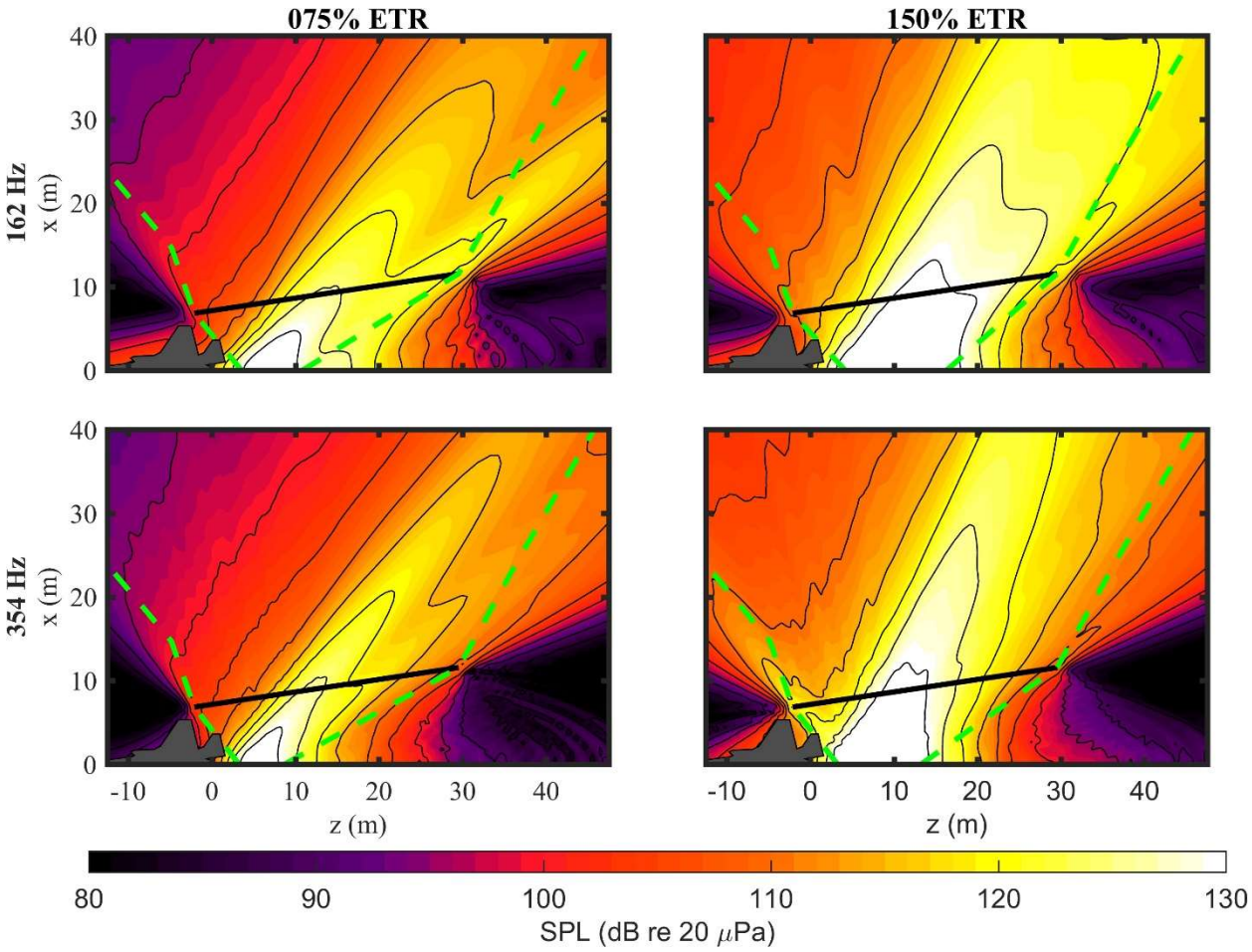

Fig. 6 Reconstructions along the $y = 0$ plane at two frequencies and engine conditions. The colored contour plots show the narrowband sound pressure level maps, the black line is the location of the input holography array, and the green dashed lines represent the region where errors are expected to be less than 2 dB (see Sec. III.B)

B. Source reconstructions

M-SONAH reconstructions at the nozzle lip line for the F-35 (the line $x = 0.5$ m, $y = 2.0$ m) can provide insight into source characteristics. Spatiospectral reconstructions to the nozzle lipline are displayed in Fig. 7, which is in the same format as Fig. 3. Each pane represents the reconstructions for 30-700 Hz at each point along the lipline. The green contour lines represent the spatial region where the levels at a given frequency are within 6 dB of the maxima at that frequency. First observation of Fig. 7 is that for a given engine condition, the peak region of the source contracts in size and shifts upstream with frequency. This frequency-dependent trend is well documented in several studies [6, 7, 10], though is shown for a wider range of engine conditions here. At 25% ETR between 300-400 Hz there seems to be two spatially separated local maxima, one of engine noise and one of aeroacoustic noise, with lower frequencies dominated by aeroacoustic noise and higher frequencies dominated by engine noise. At 50% ETR and above, the spatiospectral lobes appear less distinct than Fig. 3, though following similar patterns. This reduction in lobe clarity suggests that the multiple lobes in the field have overlapping source regions, and the fact that they separate as they propagate outward suggest that they have different acoustic source characteristics. As previously mentioned, spatial aliasing starts to appear in the reconstructions at 400 Hz, though its effect at the lipline seems to only become obvious until 500 Hz where a large aliased lobe appears downstream. Between 50% and 100% ETR, there is an enlargement of the marked 6 dB down region between 400-500 Hz, even when an aliased lobe is not observed downstream. It is

probable that the enlargement is an artifact of the spatial aliasing, as it does not follow trends measured from similar full scale military aircraft [31].

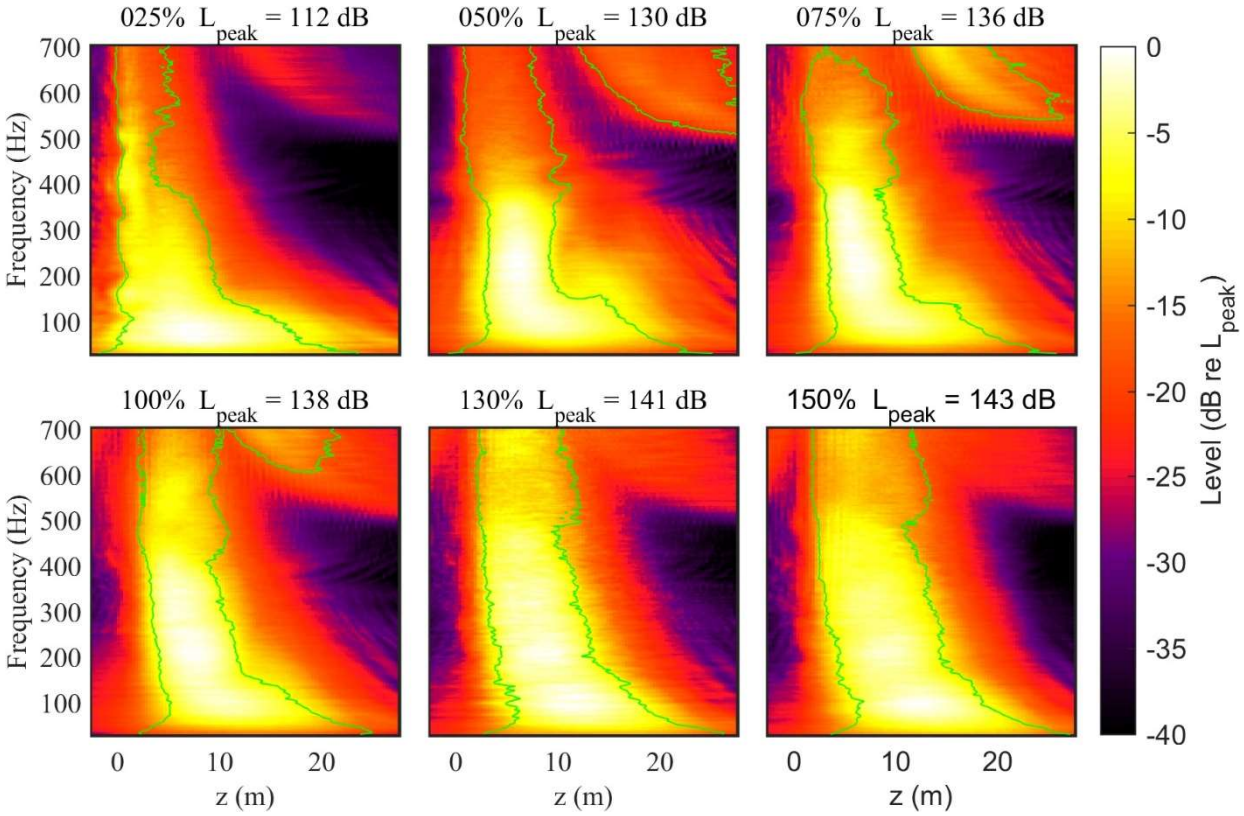

Fig. 7 Spatiospectral maps of M-SONAH reconstructions along the nozzle lipline. The green contour represents the 6 dB-down region for each frequency, which is the intersection of the green dashed lines in Fig. 4 and Fig. 6 with the nozzle lipline

C. BBSAN trends

Broadband shock-associated noise is seen in the recorded data along the holography array at upstream locations for 75, 100, 130, and 150% ETR between 400 and 700 Hz. BBSAN is seen in the field reconstructions as a radiated lobe upstream. Examples of these reconstructions are seen in Fig. 8, which shows the reconstructions along the ground plane at 450 and 549 Hz from 75% ETR to 150% ETR. At 450 Hz, there is little evidence of BBSAN at 75% ETR, but it quickly strengthens as engine condition increases. At 549 Hz BBSAN is apparent at 75% ETR and increases in strength up to 150% ETR. The directivity angle of the BBSAN (measured from the jet inlet) is larger at 549 Hz than 450Hz, and is mostly consistent across engine condition.

The reconstructions at frequencies above 400 Hz as shown in Fig. 8 are considerably noisier than low-frequency reconstructions. This has to do with the regularization step in the inversion of $\mathbf{A}^{\mathrm{H}}\mathbf{A}$. A more stringent choice of regularization parameter significantly smooths out the field, but then causes the level to be severely underestimated. The parameter used here was chosen to favor accuracy in overall level.

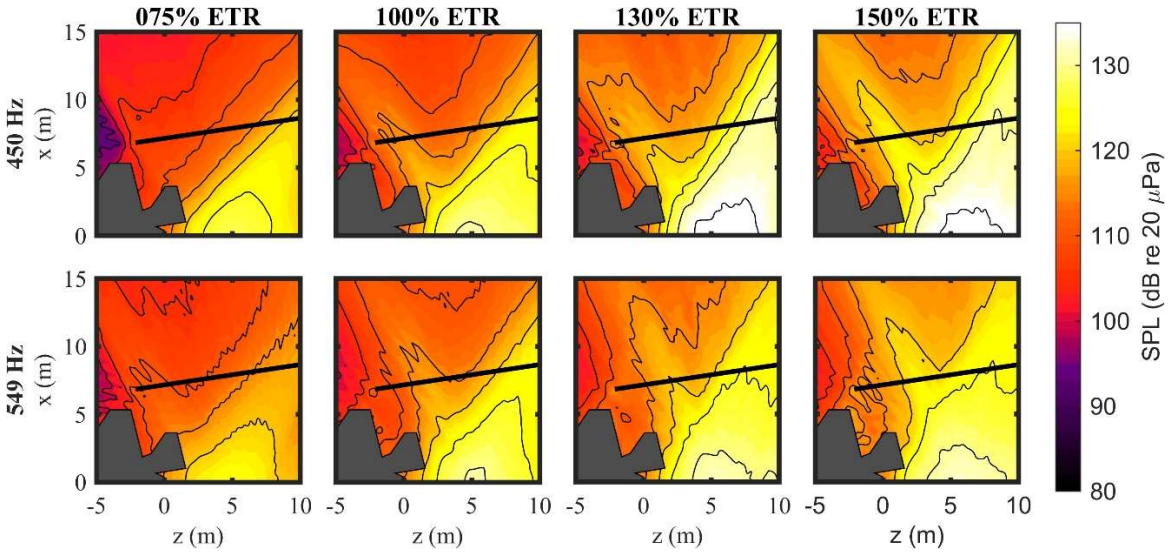

Fig. 8 Reconstructions along the ground plane of the region towards the side of the aircraft where BBSAN is apparent

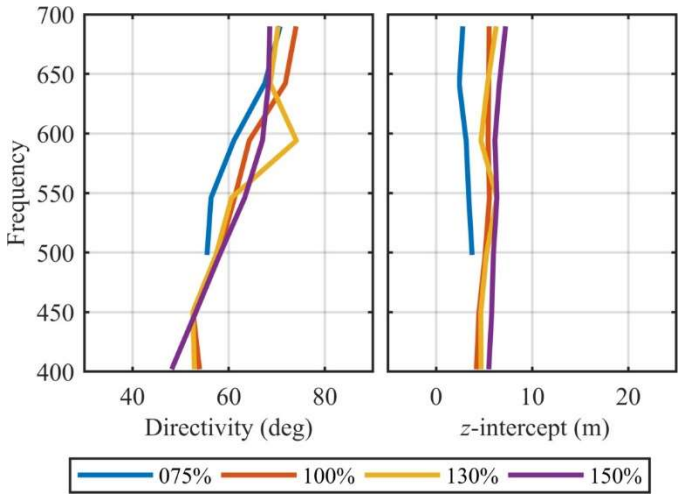

Fig. 9 Directivity and z-intercept of line traced through the BBSAN lobe for four engine conditions

Lines are fit to the reconstructed BBSAN lobes to quantify their directivity and approximate source origination point. This process is the same that is discussed in more detail in Section IV.D. First, the field is reconstructed to a fine grid of arcs of increasing radii between 12 and 46 meters. Then, the levels are normalized at each of these arcs to their corresponding maximum. The peak of the directivity of each arc is then plotted as a scatter plot on top of the two-dimensional reconstructions, and then a line is least-squares fit to points that are selected as representative of the shape of the spatial lobe. The slopes of these fitted lines are used to calculate the directivity angle of the BBSAN, and the intersection of these lines with the jet centerline ($x = 0$) give an idea of from where the BBSAN lobe originates. The results of this analysis are summarized in Fig. 9, which shows the directivity angle and z-intercept of the BBSAN noise lobe from 400 to 700 Hz for 75% -150% ETR. First, it is seen that there is little variation across engine condition, with the exception of 75% ETR. As seen in Fig. 3, the BBSAN is low level and appears at the very edge of the array. In Fig. 8, for example, the 75% ETR case at 450 Hz shows slight evidence of BBSAN being propagated into the field at the very edge of the array. It is possible that because of the low prominence of the BBSAN and incomplete coverage by the array the fitted line is less precise than at higher engine powers, where the BBSAN lobe is fully captured by the array. The placement of the origin of BBSAN in Fig. 9 is in the 6 dB down region seen in Fig. 7, though skewed towards the left. Unfortunately, aliasing present in the source reconstructions at these frequencies prevent further

analysis. The directivity angle of BBSAN noise increases with frequency across all engine conditions, which is consistent with laboratory-scale overexpanded jets [32], as well as conclusions for this aircraft by Ref. [12].

D. Multilobe trends

M-SONAH reconstructions of the field allow for tracking the development of the multiple lobes within the region of maximum radiation. As with the BBSAN lobe in Sec. IV.C, the multiple radiation lobes are traced by:

1. Reconstructing the field at a dense array of arcs around the MARP between of radii 12 and 46 meters
2. Calculating the directivity at each arc, and selecting the local maxima which have the most prominence
3. Plotting the positions of the local maxima for each arc on level contour plots similar to Fig. 6
4. Selecting which local maxima points correspond to which spatial lobe and fitting a line through those points to represent that lobe.

The dense arc arrays had radii between 12 and 46 meters and were centered on the MARP with an angular spacing of 1°. The directivity was calculated by dividing the levels at each arc with the maximum along that arc. Each arc had multiple local maxima due both to multilobe radiation patters and due to reconstructions errors, so only the three local maxima with the largest prominences were kept for each arc.

Once there was a fitted line to represent each spatial lobe at each frequency, the spatial lobes need to be connected to the spatiospectral lobes as numbered in Fig. 3. This was done by calculating the intersection point of each line with the holography array and superimposing those points on Fig. 3. Then, each point was assigned to one of the numbered spatiospectral lobes. This process contains some ambiguity in that sometimes more than one spatial local maxima at a single frequency appears to be a part of a single spatiospectral lobe. This ambiguity suggests that the spatiospectral lobes as numbered in Fig. 3 are not capturing all of the physical phenomena present. For the purposes of this paper, however, these smaller spatial fluctuations are ignored. Further analyses to isolate finer patterns than the several lobes in this paper (such as coherence analyses [23]) are ongoing.

The results of this multilobe analysis are summarized by Fig. 10 and Fig. 11. Fig. 10 shows M-SONAH reconstructions much like Fig. 6, except for more engine conditions and frequencies as well as superimposed lines that were fitted to the multiple spatial lobes. These lines are color-coded to correspond with the spatiospectral lobe numbers from Fig. 3. Blue is lobe 1, magenta is lobe 2, and cyan is lobe 3. At a single engine condition with increasing frequency, the lobes swing farther aft until they pass the aperture of the array. While that happens, new lobe(s) appears upstream and then swing aft. When each new lobe appears, it starts at a low amplitude, grows to a peak amplitude in the maximum radiation direction of the overall field, and then decays as it continues to swing aft and out of the aperture of the holography array.

As engine condition increases for a given frequency, all lobes increase in level and their directivity angle decreases, consistent with an increasing convective Mach number. Additionally, whichever lobe is farthest forward increases in level more than the others do, thus causing the forward-most lobe to increase its relative contribution to the overall field. As with the discussion of Fig. 2 and Fig. 3, it appears that the increasing contribution of the forward-most lobe is the driving factor in the change of overall directivity as engine condition increases, especially in the transition between 50% ETR and 75% ETR. The lobes appear to trace back to distinct source locations at 50% ETR, which contract and overlap as engine power increases.

To summarize trends of the individual spatiospectral lobes across engine condition and frequency, Fig. 11 takes the lines that were fit to each lobe from Fig. 10 and breaks them into two parameters: the slope of the line and the z-intercept. The slope of the line can be expressed in terms of the jet inlet angle, giving a measure of directivity for that lobe. The z-intercept of line gives an approximation to the acoustic source region corresponding to that lobe. Each point plotted on Fig. 11 is the parameter from each line that was fitted to every spatial lobe between 60 and 400 Hz. These points were then color-coded to correspond to the spatiospectral lobe numbers of Fig. 3. To show trends across frequency for each spatiospectral lobe, a line was fit to each color of points on Fig. 11. Lobe 1 (blue) begins with an aft directivity and downstream source location. As frequency increases, the changes in directivity and source location seem very sporadic, with the only consistency being that it generally stays further downstream and larger directivity angle than lobes 2-4. The large variation in lobe 1 parameters is indicative that it is probably made up of substructures, as being currently studied in Ref. [23]. Lobe 2 (magenta) has a consistent source region between 5-10 m downstream that does not change drastically with frequency. The directivity, however, generally increases with increase in frequency, with as much as a 20° increase for 50 and 75 % ETR from 150 to 400 Hz. At 130 and 150% ETR, the change in directivity is less. Lobe 3 (cyan) first appears at a higher frequency than the other two lobes and has similar trends as Lobe 2, though with a consistent decrease in z-intercept with increasing frequencies at lower engine powers.

Lobes 2 and 3 share similar z-intercepts as the BBSAN seen in Fig. 9. As engine power increases the z-intercepts for all lobes are shifted farther downstream and the directivities shift towards the sideline. In most cases the lines representing the several lobes stay in the same ordering relative to each other – lobe 1 remains the farthest downstream with lobe 3 being the farthest upstream, etc. Because of frequency limitations in the M-SONAH process applied to this experiment, only a few data points for lobe 4 are captured.

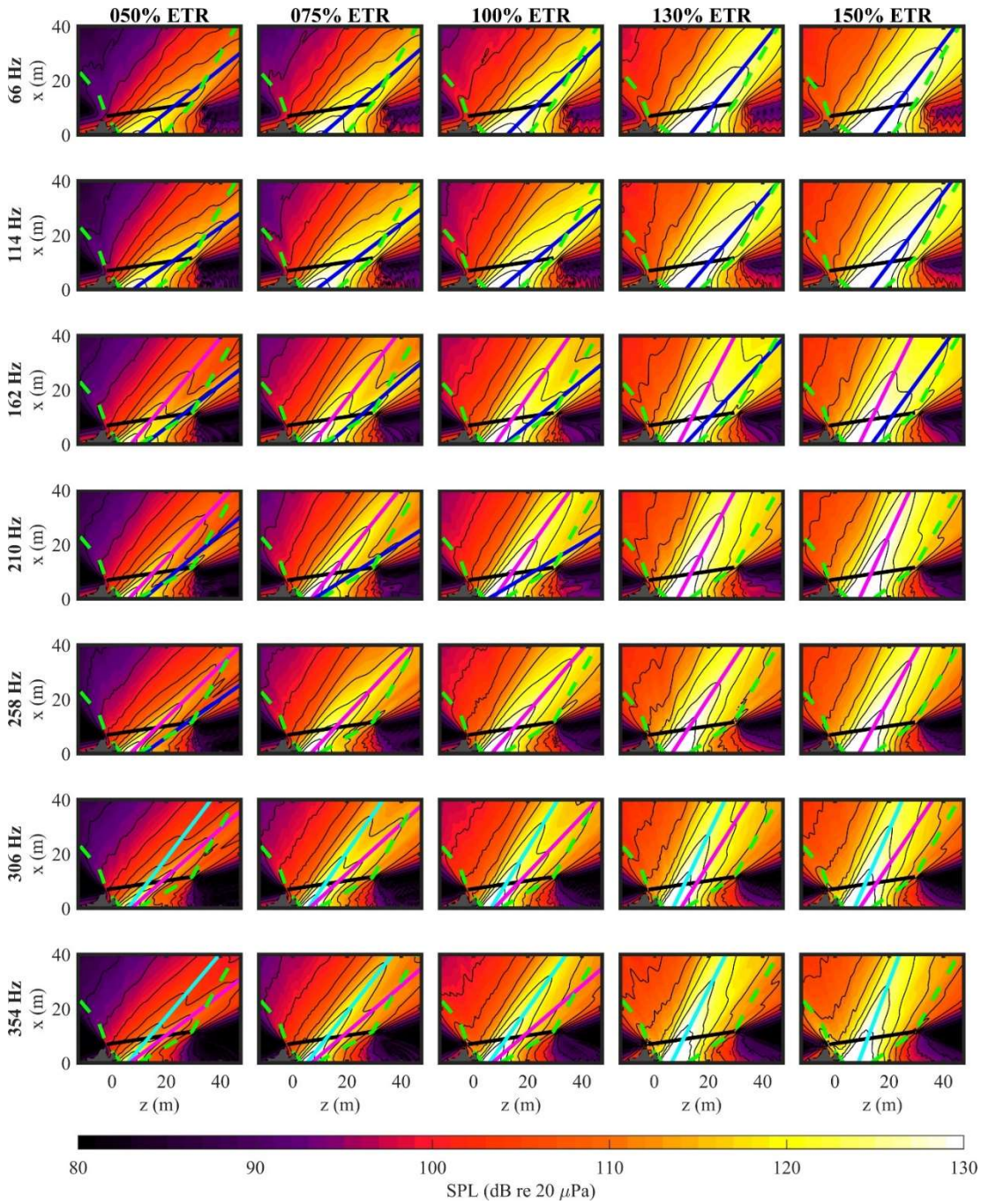

Fig. 10 M-SONAH reconstructions along the $y = 0$ plane for several frequencies and engine conditions. The blue, magenta, and cyan lines represent the lines fitted the spatial lobes, which correspond to spatiospectral lobes 1, 2 and 3 from Fig. 3.

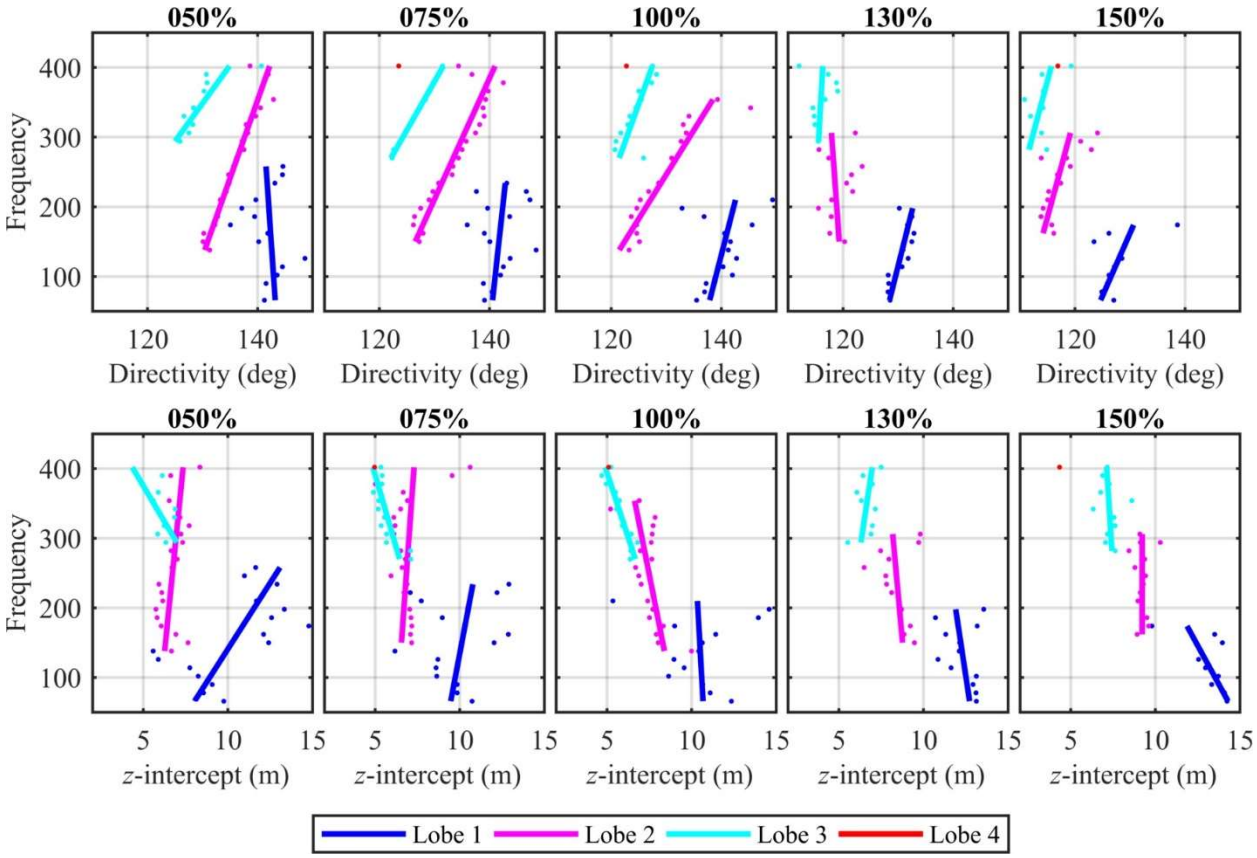

Fig. 11 Directivity angle (top row) and z-intercept (bottom row) of the lines fitted through each of the spatial radiation lobes seen in the M-SONAH reconstructions.

E. Comparison with other studies

Harker *et al.* [16] show OTO band spectra as well as correlation analyses for data collected from a ground-based linear array similar to the one in this study, though from a different aircraft with a rectangular nozzle. Fig. 2 of that paper displays the spectra as a function of distance with the OASPL, similar to Fig. 2 and Fig. 3 in this paper. The multilobe phenomenon is apparent at the afterburning engine condition, with a lobe around 100 Hz and 17 m downstream and a lobe at 250 Hz and about 10 m downstream (and maybe a third lobe at 500 Hz). Wall *et al.* [7, 33] using NAH analyses on that same dataset, images at least three spatiospectral lobes at the source. These studies show the OTO band levels on a logarithmic frequency axis instead of the narrowband levels on a linear scale as is done in this paper, which makes the lobes more difficult to see. The structure of the two lowest frequency lobes in these studies are surprisingly similar to lobes 1 and 2 as seen in Fig. 3 of this paper, which suggests that with some scaling (perhaps by Strouhal number) they could collapse into a single self-similar behavior. Unfortunately, for most military aircraft the exact flow parameters are not disclosed rendering this type of analysis difficult.

Additionally, correlation analysis in Fig. 8 of Harker *et al.* [16] show that the signals recorded in the region of maximum OASPL at afterburner have significant correlation with two different time delays, which correspond to two sets of waves with different phase speeds propagating across the array, resulting in different far-field directivities. A similar correlation analysis performed on the same dataset of this paper is shown by Fig. 12 of Ref. [23], with nearly identical results as Ref. [16]. Fig. 10 of this paper shows how the field appears to be the superposition of multiple lobes with different associated directivities, which agrees well with the correlation analyses of Refs. [16, 23].

Another look at multilobes in the OTO spectra of the same aircraft in Refs. [7, 14, 16, 17] was performed by Tam and Parrish [11], who attempted to fit large-scale turbulent structure similarity spectra to the spectra in Ref. [14]. Because of the presence of the multiple lobes, the similarity spectra do not fit well, as previously discussed by Ref.

[17]. Tam and Parrish identify two "new" noise components associated to regions in the measured spectra do not fit an ad-hoc similarity spectrum derived specifically for that study. For the first, this similarity spectrum was fit to the lower of the two peaks in the measured spectrum at $115°$, and the higher-frequency components was deemed to be a new noise source (see Fig. 22). For the second new noise source, the similarity spectrum is fit to the higher-frequency peak at $150°$ and the extra low-frequency content is called a new source (see Fig. 29). These two new noise sources are then identified as fast wave indirect combustion noise and slow wave indirect combustion noise. If indeed the aircraft under investigation has a similar multilobe structure as the F-35 as seen in this paper, then it appears the authors are attempting to fit the similarity spectrum to lobe 2, and are calling lobe 3 "fast wave indirect combustion noise" and lobe 1 "slow wave indirect combustion noise." Because of the high-resolution measurements provided by the current study of the F-35, it is clearly seen that the several lobes have similar structure and trends across engine condition and frequency. Therefore, to arbitrarily select one or two of them and attribute it to indirect combustion noise is suspect.

In an attempt to shed light on the origin of dual lobes [6, 7, 14, 17, 21, 33], Liu *et al*.[19, 20] use the JENRE large eddy simulation solver developed at the Naval Research Laboratory to simulate a supersonic jet at a temperature of 2100 K, which is comparable to those observed in high-performance jet engine exhaust. Fig. 21 a) of Ref. [20] shows a far-field spatiospectral plot which looks similar to Fig. 3, though for a larger frequency range and as a function of angle instead of downstream distance. They describe the plot as being separated into three regions: the first on the left-hand side as being dominated by BBSAN, the middle region that is the region of maximum radiation, and the further aft region that is dominated by a lower frequency component. These three regions appear very similar to Fig. 3 at afterburning engine powers, where the $z < 7$ m region is dominated by BBSAN, between 7 m and 15 m is dominated by lobes 2-5, and beyond 15m downstream is dominated by the low-frequency lobe 1. Additionally, Fig. 22 of Ref. [20] is an instantaneous pressure distribution of a plane parallel to and intersecting the jet centerline, which shows clear Mach wave radiation patterns radiating towards the middle region of the far-field data, with less regular, more turbulent-like structures radiating further aft.

Liu *et al*. [20] then hypothesize that Mach wave radiation is in fact a separate phenomenon from large-scale turbulent structure radiation, and claims that the farther-aft region dominated by the lower frequency component is in fact the turbulent structure noise. They explain: "In the past, Mach wave radiation was considered as the mechanism that large turbulence structures radiate noise [34]. This understanding probably is deduced from the observation that the difference between these two types of noises are small in laboratory-scale jets that the speeds are generally lower than those in the jet engine exhaust operated at the military and afterburner power setting". They continue by comparing several simulations of jets of the same Mach number but of different temperature ratios, where at larger temperature ratios there is a separation between Mach wave radiation and large scale turbulent mixing noise. They hypothesize that because military aircraft operate at these high temperatures they expect the different source mechanisms to separate in this manner, and the higher frequencies to be dominated by Mach wave radiation and lower frequencies by turbulent mixing noise. This hypothesis when applied to the current F-35 measurement implies that lobe 1 should be identified as large-scale turbulent structure noise, and the region enclosing lobes 2-5 should be identified as being due to Mach wave radiation. It is important to note, however, that the region in Fig. 21 of Liu *et al.* [20] that would correspond to lobes 2-5 in the current study does not appear to contain multiple lobes. Perhaps a closer look at differences between physical phenomena and simulations could provide explanations to the source mechanisms involved in generating lobes 2-5.

V. Conclusions

The sound field in the vicinity of a tied down F-35 B aircraft is examined for various engine powers, from 25% ETR to 150% ETR using an advanced holography technique (M-SONAH). The OASPLs across a linear ground array approximately parallel to the shear layer show that as engine power increases, the directivity of the field in the main radiation direction shifts towards the sideline. The maximum radiation is most unidirectional at 100% ETR then widens with the addition of afterburning effects at 130 and 150% ETR. Narrowband spatiospectral maps along the array show that the jet noise field can be described as the superposition of multiple spatiospectral lobes, and the trends in overall level with engine power are best explained by the number of lobes present and their distribution of amplitudes.

M-SONAH reconstructions of the field in the vicinity of the aircraft allow for a detailed look at the evolution of each spatiospectral lobe across frequency and engine power. At a single engine condition with increasing frequency, the lobes swing farther aft until they pass beyond the downstream extent of the array. While that happens, new lobe(s) appear upstream and then swing aft as well. As engine power increases for a fixed frequency, all lobes increase in

level and their directivity shifts toward the sideline. Additionally, whichever lobe is farthest forward increases in level more than the other lobes present at that frequency, which seems to be the largest contributor to overall trends in directivity.

The extra detail provided by this measurement of the F-35 along with the M-SONAH reconstructions makes it abundantly clear that looking at the main radiation region from high-performance military aircraft as a single phenomenon is insufficient. The paradigm needs to shift to thinking of the main radiation lobe as a superposition of smaller lobes, the trends of which across frequency and engine power dictate the trends of the overall field. The source mechanisms involved in producing the multiple radiation lobe are still unknown, though their presence at low engine powers suggest it is not combustion related [11]. Also unknown is why this phenomena appears to be more prominent in the current measurement of the F-35 than measurements of other similar aircraft [14, 15], laboratory-scale jets, and numerical simulations [19]. If a complete understanding of aeroacoustic noise from full-scale high-performance jets is desired, these questions must be answered.

Acknowledgments

The authors gratefully acknowledge funding for the measurements, provided through the F-35 Program Office and Air Force Research Laboratory. K. M. Leete was funded through by an appointment to the Student Research Participation Program at the U.S. Air Force Research Laboratory, 711th Human Performance Wing, Human Effectiveness Directorate, Warfighter Interface Division, Battlespace Acoustics Branch administered by the Oak Ridge Institute for Science and Education through an interagency agreement between the U.S. Department of Energy and USAFRL. (Distribution A: Approved for public release, distribution unlimited. F-35 PAO Cleared 05-16-2018, JSF18-529)

References

[1] Maynard, J. D., Williams, E. G., and Lee, Y. "Nearfield acoustical holography: 1. Theory of generalized holography and the development of NAH," *The Journal of the Acoustical Society of America* Vol. 78, 1985, pp. 1395-1413.

[2] Hald, J. "Basic theory and properties of statistically optimized near-field acoustical holography," *The Journal of the Acoustical Society of America* Vol. 125, 2009, pp. 967-977.

[3] Lee, M., and Bolton, J. S. "Source characterization of a subsonic jet by using near-field acoustical holography," *The Journal of the Acoustical Society of America* Vol. 121, 2007, pp. 967-977.

[4] Long, D. F. "Jet noise source location via acoustic holography and shadowgraph imagery," *AIAA Paper* Vol. 2008, No. 2888, 2008.

[5] Shah, P. N., Vold, H., and Yang, M. "Reconstruction of far-field noise using multirefrence acoustical holography measurements of high-speed jets," *AIAA Paper* Vol. 2011, No. 2772, 2011.

[6] Wall, A. T., Gee, K. L., Neilsen, T. B., Krueger, D. W., and James, M. M. "Cylindrical acoustical holography applied to full-scalle jet noise," *The Journal of the Acoustical Society of America* Vol. 136, 2014, pp. 1120-1128.

[7] Wall, A. T., Gee, K. L., Neilsen, T. B., McKinley, R. L., and James, M. M. "Military jet noise source imaging using multisource statistically optimized near-field acoustical holography," *The Journal of the Acoustical Society of America* Vol. 139, 2016, pp. 1938-1950.

[8] Leete, K. M., Gee, K. L., Neilsen, T. B., Wall, A. T., Downing, J. M., and James, M. M. "Numerical validation of using statistically optimized near-field acoustical holography in the vicinity of a high-performance military aircraft," *Proceedings of Meetings on Acoustics*, submitted 2018.

[9] Wall, A. T., Leete, K. M., Gee, K. L., Neilsen, T. B., James, M. M., and McKinley, R. L. "Preliminary investigation of multilobe fighter jet noise sources using acoustical holography," *AIAA Paper* Vol. 2017, No. 3520, 2017.

[10] James, M. M., Salton, A. R., Downing, J. M., Gee, K. L., Neilsen, T. B., Reichman, B. O., McKinley, R. L., Wall, A. T., and Gallagher, H. "Acoustic emissions from F-35A and F-35B aircraft during ground run-up," *AIAA Paper* Vol. 2015, No. 2375, 2015.

[11] Tam, C. K. W., and Parrish, S. A. "Noise of high-performance aircraft at afterburner," *Journal of Sound and Vibration* Vol. 352, 2015, pp. 103-128.

[12] Neilsen, T. B., Vaughn, A. B., Gee, K. L., Swift, S. H., Wall, A. T., Downing, J. M., and James, M. M. "Inclusion of Broadband Shock-Associated Noise in Spectral Decompositions of Noise from High-performance Military Aircraft," *AIAA Paper*, submitted 2018.

[13] Vaughn, A. B., Neilsen, T. B., Gee, K. L., Wall, A. T., Downing, J. M., and James, M. M. "Spectral decomposition of turbulent mixing and broadband shock-associated noise from a high-performance military aircraft," *The Journal of the Acoustical Society of America* Vol. 142, No. 4, 2017.

[14] Wall, A. T., Gee, K. L., James, M. M., Bradley, K. A., McInerny, S. A., and Neilsen, T. B. "Near-field noise measurements of a high performance military jet aircraft," *Noise Control Engineering Journal* Vol. 60, 2012, pp. 421-434.

[15] Tam, C. K. W., Aubert, A. C., Spyropoulos, J. T., and Powers, R. W. "On the dominant noise components of tactical aircraft: Laboratory to full Scale," *AIAA Paper* Vol. 2017, No. 3516, 2017.

[16] Harker, B. M., Neilsen, T. B., Gee, K. L., Wall, A. T., and James, M. M. "Spatiotemporal-Correlation Analysis of Jet Noise from a High-Performance Military Aircraft," *AIAA Journal* Vol. 54, No. 5, 2016, pp. 1554-1566.
[17] Neilsen, T. B., Gee, K. L., Wall, A. T., and James, M. M. "Similarity spectra analysis of high-performance jet aircraft noise," *The Journal of the Acoustical Society of America* Vol. 133, 2013. doi: 10.1121/1.4792360
[18] Liu, J., Corrigan, A., Kailasanath, K., and Gutmark, E. "Impact of chevrons on noise source characteristics in imperfectly expanded jet flows," *AIAA Paper* Vol. 2015, No. 2835, 2015.
[19] Liu, J., Kailasanath, K., and Gutmark, E. "Similarity spectral analysis of highly heated supersonic jets using large-eddy simulations," *AIAA Paper* Vol. 2017, No. 0926, 2017.
[20] Liu, J., Corrigan, A. T., Kailasanath, K., and Taylor, B. D. "Impact of the Specific Heat Ratio On the Noise Generation in a High-Temperature Supersonic Jet," *54th AIAA Aerospace Sciences Meeting*. American Institute of Aeronautics and Astronautics, 2016.
[21] Wall, A. T., Gee, K. L., Leete, K. M., Neilsen, T. B., and Stout, T. A. "Partial-field decomposition analysis of full-scale supersonic jet noises using optimized-location virtual references," *The Journal of the Acoustical Society of America*, submitted 2017.
[22] Harker, B. M., Gee, K. L., Neilsen, T. B., Wall, A. T., and James, M. M. "Beamforming-Based Wavepacket Model for Noise Enviornment Predictions of Tactical Aircraft," *AIAA Paper* Vol. 2017-4048, 2017.
[23] Swift, S. H., Gee, K. L., Neilsen, T. B., Wall, A. T., Downing, J. M., and James, M. M. " Spatiotemporal correlation analysis of jet noise from a round-nozzle supersonic aircraft," *AIAA Paper*, submitted 2018
[24] Wall, A. T., Gee, K. L., and Neilsen, T. B. "Multisource statistically optimized near-field acoustical holography," *The Journal of the Acoustical Society of America* Vol. 137, 2015, pp. 963-975.
[25] Steiner, R., and Hald, J. "Near-field acoustical holography without the errors and limitations caused by the use of spatial DFT," *International Journal of Acoustics and Vibration* Vol. 6, 2001, pp. 83-89.
[26] Hald, J. "STSF - a unique technique for scan-based Near-field Acoustic Holography without restrictions on coherence," *Bruel & Kjaer Technical Review* Vol. 1 -1989, 1989.
[27] Wall, A. T., Gee, K. L., Krueger, D. W., Neilsen, T. B., Sommerfeldt, S. D., and James, M. M. "Aperture extension for near-field acoustical holography of jet noise," *Proceedings of Meetings on Acoustics* Vol. 14, 2013, p. 065001.
[28] Williams, E. G. "Continuation of acoustic near-fields," *The Journal of the Acoustical Society of America* Vol. 113, 2003, pp. 1273-1281. doi: 10.1121/1.1528173
[29] Cho, Y. T., Bolton, J. S., and Hald, J. "Source Visualization by using statistically optimized near-field acoustical holography in cylindrical coordinates," *The Journal of the Acoustical Society of America* Vol. 118, 2005, pp. 2355-2364.
[30] Williams, E. G. "Regularization methods for near-field acoustical holography," *The Journal of the Acoustical Society of America* Vol. 110, 2001, pp. 1976-1988.
[31] Leete, K. M., Gee, K. L., Neilsen, T. B., Wall, A. T., Downing, J. M., and James, M. M. "Numerical validation of using statistically optimized near-field acoustical holography in the vicinity of a high-performance military aircraft," *The Journal of the Acoustical Society of America*, 2017.
[32] Stout, T. A., Gee, K. L., Neilsen, T. B., Wall, A. T., and James, M. M. "Source characterization of full-scale jet noise using acoustic intensity," *Noise Control Engr. J.* Vol. 63, No. 6, 2015, pp. 522 - 536.
[33] Tanna, H. K. "An experimental study of jet noise part ii: shock associated noise," *Journal of Sound and Vibration* Vol. 50, No. 3, 1977, pp. 429-444.
[34] Wall, A. T., Gee, K. L., Neilsen, T. B., Harker, B. M., McInerny, S. A., and McKinley, R. L. "Investigation of multi-lobes fighter jet noise sources using acoustical holography," *AIAA Paper*, 2015, pp. 2015-2379.
[35] Tam, C. K. W. "Mach Wave Radiation from High-Speed Jets," *AIAA Journal* Vol. 47, No. 10, 2009.